The effect of high-pressure densification on ballistic-penetration resistance of a soda-lime glass

M Grujicic[1]*, **W C Bell**[1], **B Pandurangan**[1], **B A Cheeseman**[2], **C Fountzoulas**[2], **P Patel**[2], **D W Templeton**[3], and **K D Bishnoi**[3]

[1]Department of Mechanical Engineering, Clemson University, Clemson, South Carolina, USA
[2]Army Research Laboratory – Survivability Materials Branch, Aberdeen, Maryland, USA
[3]US Army TARDEC, Warren, Michigan, USA

The manuscript was received on 17 February 2011 and was accepted after revision for publication on 17 May 2011.

DOI: 10.1177/1464420711412849

Abstract: Molecular-level modelling and simulations of the high-pressure volumetric response and irreversible densification of a prototypical soda-lime glass are first employed. The molecular-simulation results obtained were next used to modify the pressure versus degree-of-compression (the negative of volumetric strain) and yield strength versus pressure relations in order to account for the effects of irreversible densification. These relations are next used to upgrade the equation of state and the strength constitutive laws of an existing material model for glass. This was followed by a set of transient non-linear dynamics calculations of the transverse impact of a glass test plate with a solid right-circular cylindrical steel projectile. The results obtained show that irreversible densification can provide only a minor improvement in the ballistic resistance of glass and only in the case of high-velocity (ca. 1000 m/s) projectiles. Furthermore, it was demonstrated that if the key irreversible compaction parameters can be adjusted by modifications in glass chemistry and microstructure, significant improvements in the glass ballistic resistance can be attained over a relatively wide range of projectile velocities.

Keywords: glass, molecular-level modelling and simulations, high-pressure irreversible densification

1 INTRODUCTION

A public domain literature review carried out as part of this study revealed that several different materials and design strategies are currently being used in transparent ballistic-impact resistant vehicle structures (e.g. windshields, door windows, viewports, etc.). Among the most recently introduced transparent materials and technologies, the following have received the most attention: transparent crystalline ceramics (e.g. aluminium–oxynitride spinel, AlON, sapphire [**1**]), new transparent polymer materials (e.g. transparent nylon [**2**]), new interlayer technologies (e.g. polyurethane bonding layers [**3**]), and new laminate structure designs [**4**]. Despite the clear benefits offered by these materials and technologies (e.g. transparent ceramics offer a very attractive combination of high stiffness and high hardness levels, highly ductile transparent polymers provide superior fragment containing capabilities, etc.), ballistic glass remains an important constituent material in a majority of transparent impact resistant structures used today. Among the main reasons for the wide-scale use of glass, the following three are most frequently cited:

(a) glass-structure fabrication technologies enable the production of curved, large surface-area, transparent structures with thickness approaching several inches;
(b) relatively low material and manufacturing costs;
(c) compositional modifications, chemical strengthening, and controlled crystallization have demonstrated to be capable of significantly improving the ballistic properties of glass [**2**].

*Corresponding author: Department of Mechanical Engineering, Clemson University, 241 Engineering Innovation Building, Clemson, SC 29634-0921, USA.
email: mica.grujicic@ces.clemson.edu

Report Documentation Page

Form Approved
OMB No. 0704-0188

1. REPORT DATE	2. REPORT TYPE	3. DATES COVERED
MAY 2011		**00-00-2011 to 00-00-2011**

4. TITLE AND SUBTITLE	5a. CONTRACT NUMBER
The effect of high-pressure densification on ballistic-penetration resistance of a soda-lime glass	5b. GRANT NUMBER
	5c. PROGRAM ELEMENT NUMBER
6. AUTHOR(S)	5d. PROJECT NUMBER
	5e. TASK NUMBER
	5f. WORK UNIT NUMBER
7. PERFORMING ORGANIZATION NAME(S) AND ADDRESS(ES) **Clemson University,Department of Mechanical Engineering,241 Engineering Innovation Building,Clemson,SC,29634**	8. PERFORMING ORGANIZATION REPORT NUMBER
9. SPONSORING/MONITORING AGENCY NAME(S) AND ADDRESS(ES)	10. SPONSOR/MONITOR'S ACRONYM(S)
	11. SPONSOR/MONITOR'S REPORT NUMBER(S)

12. DISTRIBUTION/AVAILABILITY STATEMENT
Approved for public release; distribution unlimited

13. SUPPLEMENTARY NOTES

14. ABSTRACT

Molecular-level modelling and simulations of the high-pressure volumetric response and irreversible densification of a prototypical soda-lime glass are first employed. The molecularsimulation results obtained were next used to modify the pressure versus degree-of-compression (the negative of volumetric strain) and yield strength versus pressure relations in order to account for the effects of irreversible densification. These relations are next used to upgrade the equation of state and the strength constitutive laws of an existing material model for glass. This was followed by a set of transient non-linear dynamics calculations of the transverse impact of a glass test plate with a solid right-circular cylindrical steel projectile. The results obtained show that irreversible densification can provide only a minor improvement in the ballistic resistance of glass and only in the case of high-velocity (ca. 1000 m/s) projectiles. Furthermore, it was demonstrated that if the key irreversible compaction parameters can be adjusted by modifications in glass chemistry and microstructure, significant improvements in the glass ballistic resistance can be attained over a relatively wide range of projectile velocities.

15. SUBJECT TERMS

16. SECURITY CLASSIFICATION OF:			17. LIMITATION OF ABSTRACT	18. NUMBER OF PAGES	19a. NAME OF RESPONSIBLE PERSON
a. REPORT **unclassified**	b. ABSTRACT **unclassified**	c. THIS PAGE **unclassified**	**Same as Report (SAR)**	**18**	

The development of new glass-based transparent impact resistant structures aimed at reducing the vulnerability of protected vehicle occupants, and on-board instrumentation to various threats typically includes extensive prototyping and laboratory/field testing. These prototyping/testing programs are critical for ensuring the utility and effectiveness of the transparent impact resistant structures. However, the use of prototyping/testing programs is generally expensive, time-consuming, and involving destructive test procedures. While the role of prototyping/testing programs remains critical, they are increasingly being complemented by the corresponding computation-based modelling and simulation efforts. However, the availability of realistic physically based material models describing deformation/fracture response of ballistic glass under high-deformation-rate/high-pressure loading conditions is one of the key requirements for attaining a high level of utility and fidelity of these computation-based modelling and simulation approaches. Therefore, one of the main objectives of this study is to further advance the application of computational modelling/simulation-based engineering approaches of transparent impact-resistant structures *via* improvements in the accuracy of the existing ballistic-glass material models.

A comprehensive literature review carried out as part of this study revealed that the mechanical behaviour of glass is modelled predominantly using three distinct approaches:

(a) molecular-modelling methods;
(b) continuum-material approximations;
(c) models based on explicit crack representation.

A brief overview and the main findings for each of these three approaches are given in the remainder of this section.

1.1 Molecular-level material modelling

The first molecular-level computational investigation of glass reported in open literature can be traced back to the 1976 work of Woodcock *et al.* [**5**]. Since that time, major advances in computer technology and the introduction of high-fidelity quantum mechanics-based force fields (inter-atomic potentials) have allowed for more accurate computational modelling of glass elastic constants, strength, chemical and thermal diffusivities, surface energies, etc. Of interest to this study, a great number of researchers have investigated, using molecular modelling techniques, the propensity of various types of glass (of different chemistries and microstructures) to undergo irreversible (permanent) densification when subjected to high hydrostatic pressures on the order of 10 GPa [**6**–**8**]. The emphasis in these investigations was placed on elucidating the main atomic-level mechanisms and processes (e.g. increased coordination number, often referred to as coordination defects, creation of new metastable chemical bonds, etc.) associated with high-pressure irreversible densification of glass. In this study, on the other hand, molecular-modelling investigations of high-pressure irreversible densification of glass will be carried out in order to assess its effect on the continuum-level pressure versus degree-of-compression (the negative of volumetric strain) relation, also known as the equation of state (EOS). In addition, the ability of glass densification to act as a potent energy absorbing process, and thus, as a glass-toughening mechanism is investigated.

1.2 Continuum-level material modelling

Within the continuum-level glass models [**9**–**15**], glass is treated as a continuum material whose stiffness and strength properties may become degraded by nucleation, growth, and coalescence of cracks. The fundamental assumption in these models is that the elastic stiffness and strength degradations are the results of inelastic deformation caused by micron and submicron size cracks, and that this degradation can be quantified using a so-called 'damage tensor' whose evolution during loading can be formulated using generalized Griffith-type crack initiation and propagation criteria for brittle materials. In addition, some continuum models account for the interactions between the cracks, their coalescence, friction between fragments, competition between micro-cracking leading to fine-scale fragmentation of glass and macro-cracking giving rise to coarse fragmentation, etc. In addition to the physically based continuum-material models for glass mentioned above, the Johnson–Holmquist 2 (commonly referred to as the JH2 model [**16**]) is often used to model the behaviour of glass under high-loading rate conditions. Despite its phenomenological nature, the JH2 model has been found to often provide a reasonably good account for glass response under these loading conditions. For this reason, the JH2 model will be used in this study for coupling with the molecular modelling approaches mentioned above. Specifically, the polynomial EOS used to account for the hydrostatic/volumetric response of glass within the JH2 model will be modified to include pressure versus degree-of-compression results which will be obtained using the aforementioned molecular modelling procedure. In addition,

molecular-level results pertaining to irreversible densification-induced strengthening will be used to modify the JH2 strength constitutive law.

1.3 Explicit crack representation material models

Within this material-modelling framework, glass is treated as a linear elastic material, and its fracture is considered to take place *via* nucleation, propagation, and coalescence of discrete (rather than smeared-out/homogenized) cracks during impact [**17**]. In other words, while within the continuum modelling framework, the stiffness/strength-degrading effect of smeared-out cracks is included only implicitly; in the explicit crack representation material models, cracks are considered as discrete entities and their effect on material stiffness/strength is accounted for explicitly. When the latter type of glass models are implemented into a finite-element computational framework, crack nucleation and propagation are handled by duplicating nodes at the crack tip/front. Adaptive re-meshing is used to provide a rich enough set of possible fracture paths around the crack tip. As a crack grows, forces at newly cracked (free) surfaces are brought to zero in accordance with the Griffith criterion to account for crack growth induced unloading. This enables explicit modelling of the crack coalescence process which can lead to fragment formation. The major disadvantages of the discrete models are that they are extremely computationally expensive and become intractable as the number of cracks increases. That is, in order to capture all possible crack nucleating sites, meshes with micron-size element are ultimately required. Hence, despite the fact that inclusion of high-pressure densification effects may also be beneficial to the discrete glass models, due to their prohibitively high computational costs, they will not be considered in this study.

As demonstrated above, molecular-level, continuum-level, and discrete modelling are maturing areas of glass research which are capable of revealing complex intrinsic mechanisms and phenomena associated with deformation and fracture in glass. However, these modelling approaches are typically concerned only with the effect of the observed processes/mechanisms on the behaviour of glass at their respective length scales and practically no reports were found where the knowledge about glass behaviour at one length scale was used to improve glass models at other length scale(s). Therefore, the main objectives of this study are:

(a) to investigate and quantify (using molecular-level modelling and simulation techniques) the irreversible-densification process in soda-lime glass at high pressures;
(b) to determine if modifications in the EOS and the strength constitutive law of the JH2 continuum-material model for soda-lime glass to include the effects of high-pressure irreversible densification obtained in (a) significantly alters the mechanical response of glass under ballistic-loading conditions;
(c) to carry out a preliminary assessment of high-pressure irreversible densification as an energy-absorbing/strength-enhancing mechanism in glass.

Towards that end, molecular-level calculations are carried out first to quantify the basic pressure versus degree-of-compression relation in glass at high-pressure as this material undergoes irreversible densification. Also, molecular-level simple shear tests were carried out to assess the extent of irreversible densification-induced strengthening. The results obtained are next used to modify the JH2 EOS and strength constitutive law for glass. Then, a series of transient non-linear dynamics analyses of transverse impact of a glass test panel with a solid right-circular cylinder fragment simulating projectile (FSP) are carried out to examine (a) the extent of change in the temporal and spatial distribution of deformation and damage and (b) the resulting change in ballistic-penetration resistance brought about by the aforementioned modifications in the glass material model.

The organization of this article is as follows: a discussion of the inter-atomic force field potentials, computational cell, and the computational method used in the molecular-level simulations are all presented in section 2. Then, a brief overview of the JH2 continuum-material model for glass is provided in section 3. The main results obtained in this study (including the definition of a FSP transverse-impact problem for a glass test-panel) are presented and discussed in section 4, while the key conclusions resulting from this study are summarized in section 5.

2 MOLECULAR-LEVEL MODELLING OF GLASS

At the molecular level, soda-lime glass is treated as a discrete material consisting of:

(a) silicon (Si) and oxygen (O) atoms mutually bonded via a single covalent bond and forming a connected, non-structured/amorphous network of silica (SiO_4^{4-}) tetrahedra;
(b) oxygen anions (O^{2-}) attached as terminal functional-groups to the fragmented silica tetrahedra network;

(c) sodium cations (Na^+) dispersed between fragmented silica tetrahedra networks and ionically bonded to the oxygen anions.

To fully account for the bonding and non-bonding types of interactions between the atoms/ions listed above, one must define the respective interaction-potential functions (commonly referred to as the force-fields), as well as the associated atomic-polar and ionic charges.

While glass is an amorphous material and does not possess any long-range regularity in its atomic/molecular structure, modelling of bulk behaviour of glass is typically done at the molecular level by assuming the existence of a larger unit cell. Repetition of this cell in the three orthogonal directions (the process also known as application of the 'periodic boundary conditions') results in the formation of an infinitely large bulk-type material.

Molecular-modelling simulations typically rely on one of the following two techniques:

(a) molecular statics, the technique within which the potential energy of the molecular structure in question is minimized with respect to the position of the constituent and ions in the unit cell as well as with respect to the size and shape of the unit cell;
(b) molecular dynamics, a technique within which the Newton's equations of motion are solved for all interacting atoms an ions in the system as a function of time and the appropriate ensemble averages are used to assess/quantify various molecular-level material properties.

The discussion presented above indicates that the three main components of a molecular-level model which must be defined are:

(a) the force-fields;
(b) the initial unit cell size and shape as well as the initial positions of atoms and ions within it;
(c) the computational procedure to be employed.

A brief description of these three components used in the present molecular-level investigation of soda-lime glass behaviour under high pressures is presented in the remainder of this section.

2.1 Force-fields

While accurate simulations of a system of interacting particles (i.e. atoms or ions) generally entail the application of quantum mechanical techniques, such techniques are computationally quite expensive and are usually feasible only in systems containing up to a few hundreds of interacting particles. In addition, the main goal of simulations of the systems containing a large number of particles is generally to obtain the systems' bulk properties, which are primarily controlled by the location of atomic nuclei and the knowledge of the electronic structure, provided by the quantum mechanics techniques, is not critical. Under these circumstances, a good insight into the behaviour of a system can be obtained if a reasonable, physically based approximation of the potential (force-field) in which atomic nuclei move is available. Such a force-field can be used to generate a set of system configurations which are statistically consistent with a fully quantum-mechanical description.

As stated above, a crucial point in the molecular-level simulations of multi-particle systems is the choice of the force-fields which describe, in an approximate manner, the potential energy hyper-surface on which the atomic nuclei move. In other words, the knowledge of force-fields enables determination of the potential energy of a system in a given configuration. In general, the potential energy of a system of interacting particles can be expressed as a sum of the valence (or bond), E_{valence}, cross-term, $E_{\text{cross-term}}$, and non-bond, $E_{\text{non-bond}}$, interaction energies as

$$E_{\text{total}} = E_{\text{valence}} + E_{\text{cross-term}} + E_{\text{non-bond}} \quad (1)$$

The valence energy generally includes a bond stretching term, E_{bond}, a two-bond angle term, E_{angle}, a dihedral bond-torsion term, E_{torsion}, an inversion (or an out-of-plane interaction) term, E_{oop}, and a Urey-Bradlay term (which involves interactions between two particles bonded to a common particle), E_{UB}, as

$$E_{\text{valence}} = E_{\text{bond}} + E_{\text{angle}} + E_{\text{torsion}} + E_{\text{oop}} + E_{\text{UB}} \quad (2)$$

A schematic explanation of the first four types of valence atomic interactions is given in Fig. 1.

The cross-term interacting energy, $E_{\text{cross-term}}$, accounts for the effects such as bond length and

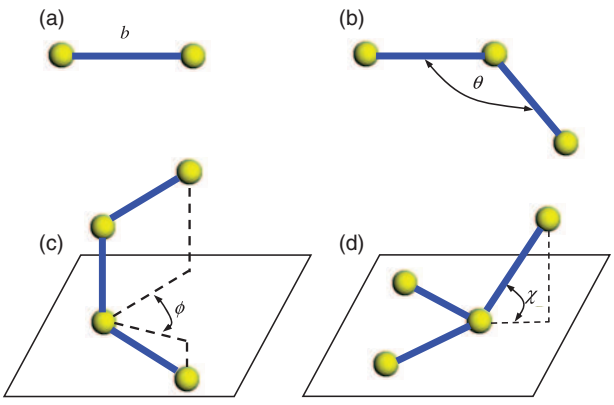

Fig. 1 A schematic of (a) stretch, (b) angle, (c) torsion, and (d) inversion valence atomic interactions

angle changes caused by the surrounding atoms and generally includes:

(a) stretch–stretch interactions between two adjacent bonds, $E_{\text{bond–bond}}$;
(b) stretch–bend interactions between a two-bond angle and one of its bonds, $E_{\text{bond–angle}}$;
(c) bend–bend interactions between two valence angles associated with a common vertex particle, $E_{\text{angle–angle}}$;
(d) stretch–torsion interactions between a dihedral angle and one of its end bonds, $E_{\text{end\_bond–torsion}}$;
(e) stretch–torsion interactions between a dihedral angle and its middle bond, $E_{\text{middle\_bond–torsion}}$;
(f) bend–torsion interactions between a dihedral angle and one of its valence angles, $E_{\text{angle–torsion}}$;
(g) bend–bend–torsion interactions between a dihedral angle and its two valence angles; $E_{\text{angle–angle–torsion}}$;

terms as

$$E_{\text{cross–term}} = E_{\text{bond–bond}} + E_{\text{angle–angle}} + E_{\text{bond–angle}} + E_{\text{end\_bond–torsion}} + E_{\text{middle\_bond–torsion}} + E_{\text{angle–torsion}} + E_{\text{angle–angle–torsion}} \quad (3)$$

The non-bond interaction term, $E_{\text{non-bond}}$, accounts for the interactions between non-bonded particles and includes the van der Waals energy, E_{vdW}, the Coulomb electrostatic energy, E_{Coulomb}, and the hydrogen bond energy, $E_{\text{H-bond}}$, as

$$E_{\text{non–bond}} = E_{\text{vdW}} + E_{\text{Coulomb}} + E_{\text{H–bond}} \quad (4)$$

Particle interactions in the soda-lime glass system under investigation are modelled using COMPASS (condensed-phased optimized molecular potential for atomistic simulation studies), the first *ab initio* force-field that enables an accurate and simultaneous prediction of various gas-phase and condensed-phase properties of organic and inorganic materials [**18**, **19**]. The COMPASS force-field uses the following expression for various components of the potential energy

$$E_{\text{bond}} = \sum_b \left[K_2(b-b_0)^2 + K_3(b-b_0)^3 + K_4(b-b_0)^4\right] \quad (5)$$

$$E_{\text{angle}} = \sum_\theta \left[H_2(\theta-\theta_0)^2 + H_3(\theta-\theta_0)^3 + H_4(\theta-\theta_0)^4\right] \quad (6)$$

$$E_{\text{torsion}} = \sum_\phi \left[V_1\left[1-\cos\left(\phi-\phi_1^0\right)\right] + V_2\left[1-\cos\left(2\phi-\phi_2^0\right)\right] + V_3\left[1-\cos\left(3\phi-\phi_3^0\right)\right]\right] \quad (7)$$

$$E_{\text{oop}} = \sum_x K_x \chi^2 \quad (8)$$

$$E_{\text{bond–bond}} = \sum_b \sum_{b'} F_{bb'}(b-b_0)\left(b'-b_0'\right) \quad (9)$$

$$E_{\text{angle–angle}} = \sum_\theta \sum_{\theta'} F_{\theta\theta'}(\theta-\theta_0)\left(\theta'-\theta_0'\right) \quad (10)$$

$$E_{\text{bond–angle}} = \sum_b \sum_\theta F_{b\theta}(b-b_0)(\theta-\theta_0) \quad (11)$$

$$E_{\text{end\_bond–torsion}} = \sum_b \sum_\phi F_{b\phi}(b-b_0)[V_1\cos\phi + V_2\cos 2\phi + V_3\cos 3\phi] \quad (12)$$

$$E_{\text{middle\_bond–torsion}} = \sum_{b'} \sum_\phi F_{b'\phi}\left(b'-b_0'\right) \times [F_1\cos\phi + F_2\cos 2\phi + F_3\cos 3\phi] \quad (13)$$

$$E_{\text{angle–torsion}} = \sum_\theta \sum_\phi F_{\theta\phi}(\theta-\theta_0) [V_1\cos\phi + V_2\cos 2\phi + V_3\cos 3\phi] \quad (14)$$

$$E_{\text{angle–angle–torsion}} = \sum_\phi \sum_\theta \sum_{\theta'} K_{\phi\theta\theta'} \times \cos\phi(\theta-\theta_0)\left(\theta'-\theta_0'\right) \quad (15)$$

$$E_{\text{Coulomb}} = \sum_{i>j} \frac{q_i q_j}{\varepsilon r_{ij}} \quad (16)$$

$$E_{\text{vdW}} = \sum_{i>j} \left[\frac{A_{ij}}{r_{ij}^9} - \frac{B_{ij}}{r_{ij}^6}\right] \quad (17)$$

where b and b' are the bond lengths, θ the two-bond angle, φ the dihedral torsion angle, χ the out of plane angle, q the atomic charge, ϵ the dielectric constant, and r_{ij} the i–j atomic separation distance. b_0, K_i ($i=2$–4), θ_0, H_i ($i=2$–4), φ_i^0 ($i=1$–3), V_i ($i=1$–3), $F_{bb'}$, b_0', $F_{\theta\theta'}$, θ_0', $F_{b\theta}$, $F_{b\varphi}$, $F_{b'\varphi}$, F_i ($i=1$–3), $F_{\theta\varphi}$, $K_{\varphi\theta\theta'}$, A_{ij}, and B_{ij} are the material-system dependent parameters implemented into Discover [**20**], the atomic simulation program used in this study.

2.2 Computational cell

In the molecular-level modelling portion of this study, a 2916-particle computational cell was created with a chemical composition of $(Na_2O)_{0.15}$ $(SiO_2)_{0.85}$. The molecular-level unit cell was constructed with a cubic geometry having a uniform edge-length of 3.347 nm. An amorphous cell of sodium silicate glass was thus created with a density of 2.613 g/cm^3. The three edges (*a*, *b*, and *c*) of the cell were aligned, respectively, with the three coordinate axes (*x*, *y*, and *z*). To create a bulk-material environment for the particles, periodic boundary conditions were applied to all six faces of the unit cell.

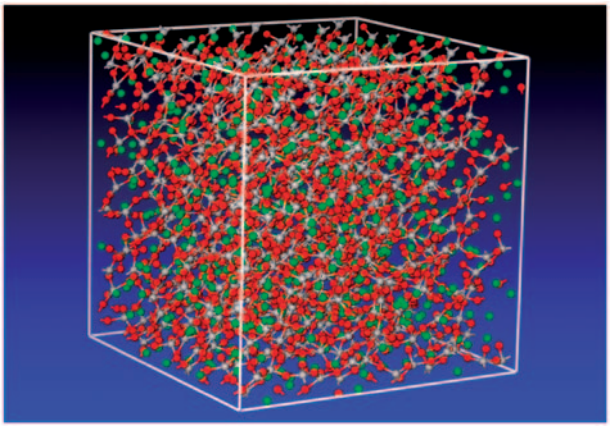

Fig. 2 The computational unit cell for soda-lime glass molecular-level simulations used in this study

To create the initial particle configuration in the unit cell, the Visualizer [**21**] from Accelrys was first used to construct a short silica-chain fragment. The fragment was then 'grown' by a duplicate-and-attach process using the same program. The resulting silica network was next used within the Amorphous Cell program [**22**] from Accelrys to randomly populate the computational cell while ensuring that the target material density of 2.613 g/cm^3 was attained. Finally, sodium cations were added to obtain an electrically neutral system of particles. An example of a typical molecular-level topology within a single unit cell is displayed in Fig. 2. When creating the computational cell for the subject material (soda-lime glass in the present case), one should try to answer the question as to how representative is the computational cell of the material in question. Typically, the size of the computational cell, i.e. the number of the constituent atoms analysed is a compromise between the available computer resources (CPU time, primarily) and a desire to maximize the size of the computational model. The reason that the computational-model size should be maximized is that the effect of the periodic boundary conditions which artificially introduce configurational-order into an amorphous/disordered solid should be minimized. To qualify the computational cell used in this study, few simulations are carried out using a computational cell with a doubled-edge length. Since no statistically significant differences in the key results were seen for the two choices of the unit cell, it is concluded that the computational cell used is adequate.

2.3 Computational method

High-pressure irreversible densification of glass was studied using a conventional *NPT* dynamics method within the Discover program [**20**] from Accelrys, where N (the number of particles), P (pressure), and T (temperature) are the system variables that are held constant or ramped in a controlled manner during compression-simulation runs. The equations of motion were integrated using the velocity Verlet algorithm with a time step of 1.0 fs. To comply with typical ballistic-impact loading conditions, pressure was ramped linearly at a rate of 0.3 GPa/ps. Pressure ramping was accomplished by 3 GPa discrete increments in pressure followed by 10.0 ps equilibration times at a given pressure level. Temperature, on the other hand was held constant at a value of 300 K using a Nosé Thermostat [**23**].

At the end of equilibration at each pressure level, the average material density was computed from the corresponding pair-correlation functions. This procedure yielded the sought pressure versus degree-of-compression relation for the pressurization portion of a loading cycle. To determine the corresponding pressure versus degree-of-compression relation during the depressurization portion of a loading cycle, pressure was decreased in a similar manner as discussed above. Differences in the pressure versus degree-of-compression relations for the pressurization and depressurization portions of the loading cycle are then used to quantify the extent of high-pressure irreversible densification of glass.

As will be explained later in more detail, irreversible densification can affect the ballistic-penetration of glass not only via increased density but also through the associated changes in the material strength. To assess the extent of densification-induced strengthening, molecular-level simple-shear tests were carried out. These tests were conducted through the use of a Discover input file which was written in a basic tool command language (BTCL). This enabled the use of a scripting engine that provides very precise control of simulation runs, e.g. a cell deformation to be carried out in small steps each followed by energy minimization. The minimization portion of the molecular-level simple shear tests was carried out using a combination of three (steepest descent, conjugate gradient, and Newton's) potential-energy minimization algorithms within Discover [**20**]. These algorithms are automatically activated/deactivated as the molecular-level configuration approaches its energy minimum (i.e. the steepest descent method is activated at the beginning of the energy-minimization procedure, while the Newton's method is utilized in the past stages of the simulation).

3 JH2 CONTINUUM-MATERIAL MODEL

To completely define a continuum-level material dynamic model, the relationships between the flow

variables (pressure, mass-density, energy-density, temperature, etc.) must be specified. These relations typically involve:

(a) an EOS;
(b) a strength equation;
(c) a failure equation;
(d) an erosion equation.

These equations arise from the fact that, in general, the total stress tensor can be decomposed into a sum of a hydrostatic stress (pressure) tensor (which causes a change in the volume/density of the material) and a deviatoric stress tensor (which is responsible for the shape change of the material). An EOS then is used to define the corresponding functional relationship between pressure, mass density (degree-of-compression), and internal energy density (temperature). Likewise, a strength relation is used to define the appropriate equivalent plastic strain, equivalent plastic strain rate, and temperature dependencies of the materials yield strength. This relation, in conjunction with the appropriate yield-criterion and flow-rule relations, is used to compute the deviatoric part of stress under elastic–plastic loading conditions. In addition, a material model generally includes a failure criterion (i.e. an equation describing the hydrostatic or deviatoric stress and/or strain condition(s) which, when met, causes the material to fracture and lose its ability to support, abruptly in the case of brittle materials or gradually in the case of ductile materials, normal and shear stresses). Such a failure criterion in combination with the corresponding material-property degradation and the flow-rule relations governs the evolution of stress during failure. The erosion equation is generally intended for eliminating numerical difficulties arising from highly distorted Lagrange cells. Nevertheless, the erosion equation is often used to provide additional material failure mechanisms, especially in materials with limited ductility.

To summarize, the EOS along with the strength and failure equations (as well as with the equations governing the onset of plastic deformation and failure and the plasticity and failure induced material flow) enable assessment of the evolution of the complete stress tensor during a transient non-linear dynamics analysis. Such an assessment is needed in order to solve the governing (mass, momentum, and energy) conservation equations. It is important to note that separate evaluations of the pressure and the deviatoric stress enable inclusion of the non-linear effects in the EOS. Generally, these effects are shock related but, in this study, they will be, at least partly, attributed to the phenomenon of high-pressure irreversible densification.

In this study, glass was modelled using the JH2 brittle-material model [**24**, **25**]. The JH2 model is a phenomenological model which postulates the existence of two terminal glass states: (a) an intact material and (b) a failed material. The two material states are weighted by a single scalar variable called damage, D, whose evolution is governed by an inelastic (plasticity-like deformation model). The JH2 model includes a polynomial-type EOS, a strength model (based on the von Mises yield criterion, normality flow rule and a pressure and strain-rate hardening constitutive relation), a progressive failure model, and an instantaneous geometric strain-based erosion criterion. The values of all the JH2 material-model parameters for soda-lime float glass are available in the ANSYS/Autodyn materials library [**26**]. Further details of the JH2 model for brittle materials are provided in the remainder of this section.

3.1 Polynomial EOS

Within the JH2 polynomial EOS, the effect of internal-energy density is neglected and the pressure versus degree-of-compression in a damage-free material is defined as

$$P = K_1\mu + K_2\mu^2 + K_3\mu^3, \quad \mu > 0 \quad \text{(hydrostatic compression)} \tag{18}$$

and

$$P = K_1\mu, \quad \mu < 0 \quad \text{(hydrostatic tension)} \tag{19}$$

where degree-of-compression is $\mu = (\rho/\rho_0 - 1)$ and ρ the current density, while ρ_0 (the reference density), K_1 (the bulk modulus), and K_2 and K_3 the material-specific constants.

After glass has begun to accumulate damage (i.e. when the extent of damage is no longer zero, $D > 0$), equation (18) has to be upgraded to include the effect of bulking. Bulking is a phenomenon associated with the fact that fragments of fractured materials are not generally fully conformable and, consequently fractured material is associated with a larger volume (a lower density at a constant pressure) than the damage-free material. The bulking modified polynomial EOS is then given by [**26**]

$$P = K_1\mu + K_2\mu^2 + K_3\mu^3 + \Delta P, \quad \mu > 0 \tag{20}$$

where the bulking-induced pressure increment, ΔP, is determined from energy considerations and varies from zero at $D = 0$ to ΔP_{max} at $D = 1.0$. Assuming that a fraction of the internal elastic energy decrease (due to decrease in deviatoric stresses in the material) is converted to an increase in potential internal energy, the bulking induced pressure increment ΔP at a time

$t + \Delta t$ can be represented in terms of ΔP at the time t as

$$\Delta P(t+\Delta t) = -K\mu(t+\Delta t) + \sqrt{(K_1\mu(t+\Delta t) + \Delta P(t))^2 + 2\beta K_1 \Delta U} \quad (21)$$

where ΔU is the decrease in deviatoric elastic energy due to damage induced yield-strength reduction and β the fraction of the deviatoric elastic energy converted to hydrostatic potential/elastic energy. The decrease in deviatoric elastic energy is given by

$$\Delta U = U_t - U_{t+\Delta t} \quad (22)$$

where

$$U_t = \frac{\sigma_t^2}{6G} \quad (23)$$

The parameters σ_t and G appearing in equation (23) are the actual yield strength and the damage-free shear modulus of the glass material, respectively.

3.2 Strength model

Within the JH2 strength model [**24**, **25**], the normalized yield strength is defined as a damage-weighted rule of mixtures of the corresponding damage-free and fractured yield strengths as

$$\sigma^* = \sigma_i^* - D(\sigma_i^* - \sigma_f^*) \quad (24)$$

where subscripts i and f are used to denote intact and fractured material states and the superscript * indicates that the corresponding yield strength is normalized by the Hugoniot elastic limit (HEL; uni-axial stress) yield strength, that is

$$\sigma^* = \frac{\sigma}{\sigma_{\text{HEL}}} \quad (25)$$

The normalized yield strengths σ_i^* and σ_f^* are also defined in the same manner as σ^*. The normalized (pressure and strain rate dependent, ideal-plastic) yield strength of the damage-free material, σ_i^*, and the fractured material, σ_f^*, are, respectively, given by

$$\sigma_i^* = A(P^* + T^*)^N(1 + C\ln\dot{\varepsilon}^*) \quad (26)$$

$$\sigma_f^* = B(P^*)^M(1 + C\ln\dot{\varepsilon}^*) \quad (27)$$

where A, B, C, M, N, and σ_{HEL} appearing in equations (25) to (27) are all material-specific constants while P^* and T^* are, respectively, defined as

$$P^* = \frac{P}{P_{\text{HEL}}} \quad (28)$$

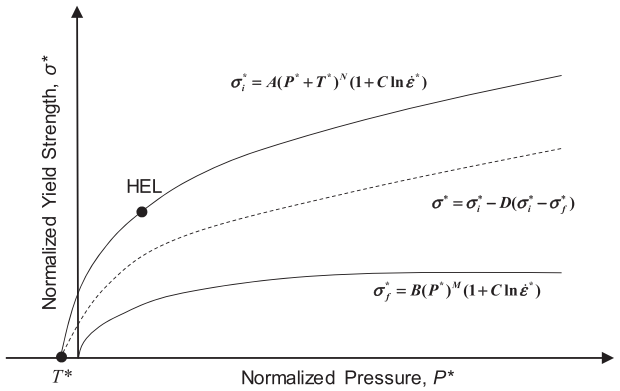

Fig. 3 A schematic of the JH2 strength model in the normalized yield strength, σ*, versus normalized pressure, P^*, plane

and

$$T^* = \frac{T}{P_{\text{HEL}}} \quad (29)$$

where P and T are the actual pressure and the maximum hydrostatic tensile pressure that the glass material can withstand, respectively, and P_{HEL} the pressure at HEL. A schematic of the JH2 strength model in the normalized yield strength versus normalized pressure plane is displayed in Fig. 3.

As shown in reference [**25**], P_{HEL} and σ_{HEL} are related to the (uni-directional shockwave-based) uniaxial-strain compressive strength, HEL, as: $\text{HEL} = P_{\text{HEL}} + \frac{2}{3}\sigma_{\text{HEL}}$. Since both P_{HEL} and σ_{HEL} are dependent on the compression ratio at the HEL, both these parameters can be determined from HEL. Finally, the dimensionless material strain rate, $\dot{\varepsilon}^*$, appearing in equations (28) and (29) is defined as

$$\dot{\varepsilon}^* = \frac{\dot{\varepsilon}}{\dot{\varepsilon}_0} \quad (30)$$

where $\dot{\varepsilon}$ is the actual strain rate and $\dot{\varepsilon}_0$ the reference strain rate (typically set to $1.0\,\text{s}^{-1}$).

3.3 Failure model

Within the JH2 failure model [**24**, **25**], the evolution/accumulation of damage is defined as

$$D = \sum \frac{\Delta\varepsilon_p}{\varepsilon_p^f} \quad (31)$$

where $\Delta\epsilon_p$ is the increment in equivalent plastic strain with an increment in loading and the failure strain ε_p^f is a pressure-dependent equivalent fracture strain, which is defined as

$$\varepsilon_p^f = D_1(P^* + T^*)^{D2} \quad (32)$$

where D_1 and D_2 are material-specific constants.

Within the JH2 failure model, fracture occurs when either damage reaches a critical value of 1.0 or when negative pressure reaches a value of *T*. Fracture material has no ability to support any negative pressure, while its ability to support shear is defined by equation (27).

3.4 Erosion model

Within the finite-element computational framework, numerical difficulties may arise from excessive distortion of the elements. To overcome these difficulties, an erosion algorithm, which at a predefined level of strain removes the excessively distorted elements, while transferring the momentum associated with the removed nodes to the remaining nodes. Following our prior work [**27**–**30**], the erosion criterion is defined by prescribing a critical value for the instantaneous geometrical equivalent strain.

4 RESULTS AND DISCUSSION

4.1 Molecular-level analysis of high-pressure densification of glass

In this section, a brief summary of the molecular-level calculations of glass response to high pressure is provided. While this portion of the work yielded numerous results, only the ones directly related to the potential role of high-pressure irreversible densification in improving impact/penetration resistance of glass are presented and discussed in greater detail. Other results are discussed only qualitatively.

4.1.1 Molecular-level topology

A detailed examination of the molecular-level topology after subjecting the unit-cell to high pressures revealed distinct differences depending on whether the maximum pressure was below or above *ca.* 4 GPa.

Pressures below ~4 GPa: Molecular modelling of glass pressurization/depressurization revealed that when glass is exposed to pressures not exceeding *ca.* 4 GPa, no detectable irreversible changes generally take place in its molecular topology. Closer examination of the atomic structure at different pressure levels between 0 and 4 GPa revealed as follows.

1. The presence of 'active regions' within which atoms may occasionally undergo large displacements/jumps (*ca.* 0.1 nm). These atomic displacements (the results not shown for brevity) were found to involve coordinated motion of at least a dozen atoms and to be accompanied by abrupt changes in the average potential energy.
2. In most cases, atomic rearrangement described in (a) appears to be associated with low-frequency transition of the active regions between two distinct 'equilibrium' states (of comparable potential energy). These findings are in complete agreement with those found by Trachenko and Dove [**7**] who termed this phenomenon as Double Well Potential and the associated low-frequency transition/vibrational mode as the 'floppy mode'.
3. While pressurization up to 4 GPa did not yield any permanent changes in the molecular topology, the locations of the active regions were found to change with pressure. That is, the regions active at one pressure level may become inactive at another pressure level while, at the same time other previously inactive regions would become active.

Pressures above ~4 GPa: When the computational cell is subjected to pressure exceeding *ca.* 4 GPa and subsequently depressurized to zero pressure, permanent changes in the glass molecular topology were normally observed. These molecular topology changes were accompanied by a permanent density increase in the order of 3–7 per cent. An example of typical results obtained in this portion of the work is given in Figs 4(a) to (d), where oxygen atoms/anions are displayed in red and silicon atoms are shown in grey (as well green, pink, and yellow highlighting), while sodium cations are omitted for clarity. To aid in visualization/interpretation of the topological changes experienced by glass during high-pressure loading/unloading cycles, only a 30–40-atom exemplary region of computational cell was monitored in Figs 4(a) to (d). The molecular level topologies displayed in these figures pertain respectively to:

(a) high-pressure state, Fig. 4(a);
(b) high-pressure state after a prolonged (20 ps) relaxation period, Fig. 4(b);
(c) ambient pressure state resulting from depressurization of state (a), Fig. 4(c);
(d) ambient pressure state resulting from depressurization of state (b), Fig. 4(d).

It should be noted that the results displayed in Fig. 4(c) are essentially identical to those in the initial configuration prior to loading. A closer examination of the molecular-level topology results displayed in these figures revealed as follows.

1. Pressurization alters not only molecular-level topology, but also changes the bonding structure and increases the average coordination number (of mainly Si atoms). This can be seen by comparing the results displayed in Figs 4(a) and (c). It should be noted here, that the results displayed in Fig. 4(c)

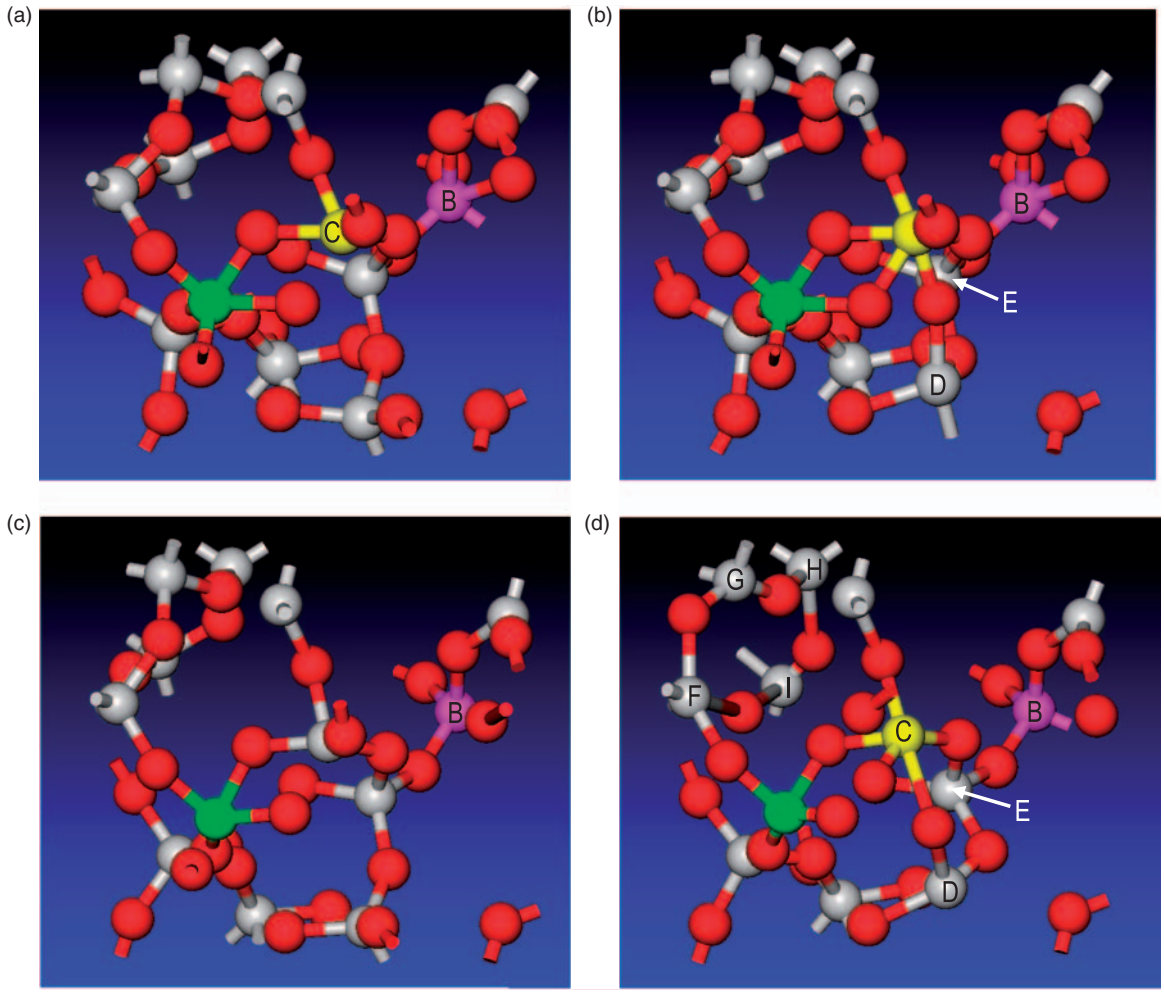

Fig. 4 The molecular level topologies pertaining to: (a) high-pressure state; (b) high-pressure state after a prolonged (20 ps) relaxation period; (c) ambient pressure state resulting from depressurization of state (a); and (d) ambient pressure state resulting from depressurization of state (b). See text for explanation

are used in place of the initial molecular-level topology results. In these figures, it is seen that silicon atoms labelled *A* and *B* change their fourfold coordination to fivefold coordination upon pressurization.

2. As implied earlier, if the depressurization is carried out without allowing the material to relax at high pressures, the molecular level configuration obtained at the ambient pressure is effectively identical to the initial configuration, Fig. 4(c). Thus, in the resultant ambient-pressure configuration, most silicon atoms regain their fourfold coordination.
3. Increased duration of the exposure of glass to high pressure results in continued changes in the molecular-level topology and bond structure. This can be seen by comparing the results displayed in Figs 4(a) and (b). These figures show that relaxation of glass leads to the *C*-label silicon atom acquiring a fivefold coordination while, at the same time smaller size Si–O rings are being formed. For example, a twofold ring is formed involving the *A* and *C* silicon atoms, while a threefold ring involving the *C*-, *D*-, and *E*-labelled Si atoms also appears, Fig. 4(b). These changes in the molecular-level topology of glass are a manifestation of its relaxation to a material state that is energetically preferred at high pressures.
4. Upon depressurization of glass which was relaxed at high pressures, some changes in the molecular-level topology and the bonding structure are observed. However, the initial material state is not restored. That is, the material has undergone permanent changes in its molecular level topology, bond structure, and density. This can be seen by comparing results displayed in Figs 4(c) and (d). These figures show that while *A*- and *B*-labelled silicon atoms regain their fourfold coordination upon depressurization to ambient pressure, the *C*-labelled silicon atom retains its fivefold

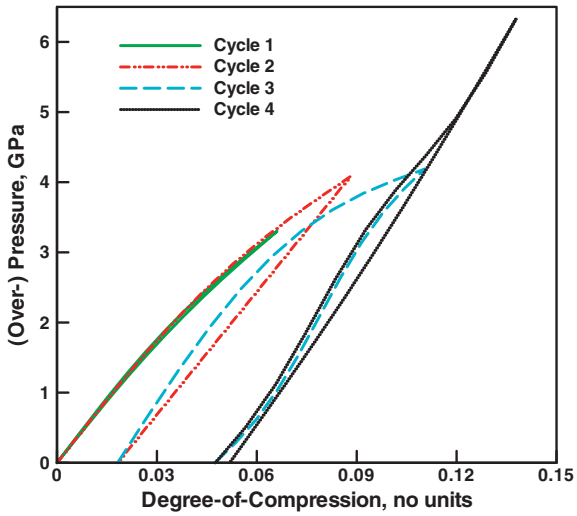

Fig. 5 Typical pressure versus degree-of-compression results obtained in the present molecular-level analysis of repeated pressurization/depressurization simulations. In each loading cycle, pressurization was carried out to a higher peak pressure followed by a complete depressurization (i.e. to the atmospheric pressure)

coordination, Figs 4(b) and (d). Thus, the average coordination number of silicon atoms in the relaxed-then-depressurized state, Fig. 4(d), is higher than that in the initial configuration, Fig. 4(c). Furthermore, while the aforementioned twofold Si–O ring was broken upon depressurization, the threefold ring involving the *C*-, *D*-, and *E*-labelled silicon atoms survived this process. In addition, a new fourfold ring involving the Si atoms labelled *F*, *G*, *H*, and *I* was formed. The threefold and fourfold rings were not present in the initial molecular-level configuration, Fig. 4(c).

4.1.2 Pressure versus degree-of-compression relation

An example of the typical pressure, P versus degree-of-compression, μ results obtained in the present molecular-level analysis of high-pressure irreversible densification of glass is displayed in Fig. 5. The results in Fig. 5 show four loading pressurization/depressurization cycles. The first cycle does not result in any irreversible densification of glass since the maximum pressure attained is not high enough. The second and third cycles yield irreversible densification and reveal that this process is associated with a nearly constant *ca.* 4 GPa pressure level. During the past cycle, irreversible densification is completed so that glass behaves as a perfectly elastic material when subjected to any further loading.

To summarize, the examination of the results displayed in Fig. 5 revealed the following three important findings: (a) irreversible densification begins at a pressure level of ~4 GPa and proceeds to full densification at a nominally constant pressure; (b) irreversible densification is associated with a density increase of *ca.* 5 per cent; and (c) the average rate of change of pressure with density (which scales with the material bulk modulus) is not significantly different (and will be assumed equal) in the pre- and post-densification glass states.

It should be noted that the aforementioned findings (a) and (c) were found not to be very sensitive to the random selection of the initial molecular-level configuration of glass. On the other hand, the extent of irreversible densification was found to vary in a 3–7 per cent range depending on the choice of this configuration. This observation suggests that the volumetric response of the soda-lime glass in its pre- and post-irreversible compaction states as well as the pressure at which irreversible compaction initiates/proceeds are functions of the global/assembly level thermodynamic state of the material while the extent of the irreversible densification is more sensitive to the local-details of the material microstructural state.

4.1.3 Densification-induced material strengthening

As mentioned earlier, molecular level simple-shear tests were carried out in order to assess the extent of irreversible densification-induced strengthening of glass. Towards that end, shearing of the computational cell was carried out in small increments followed by energy minimization with respect to the atomic positions. An example of the typical molecular-level topology evolution accompanying these tests is displayed in Figs 6(a) to (d). To help prevent the computational crystal from settling into a nearby metastable higher-energy configuration, a 10 000-step 300 K *NVT* molecular dynamics (equilibration) run was introduced between the cell shearing and the energy minimization steps. This procedure yielded a plot of the potential energy increase (relative to that in the initial optimized computational cell) versus the shear angle of the computational cell. The shear angle gradient of the potential energy increase divided by the constant unit cell volume is then used to define the material shear strength. This procedure revealed that the shear strength of glass in the irreversibly compacted state is higher by a factor of *ca.* 1.5 relative to the strength of glass in the initial state.

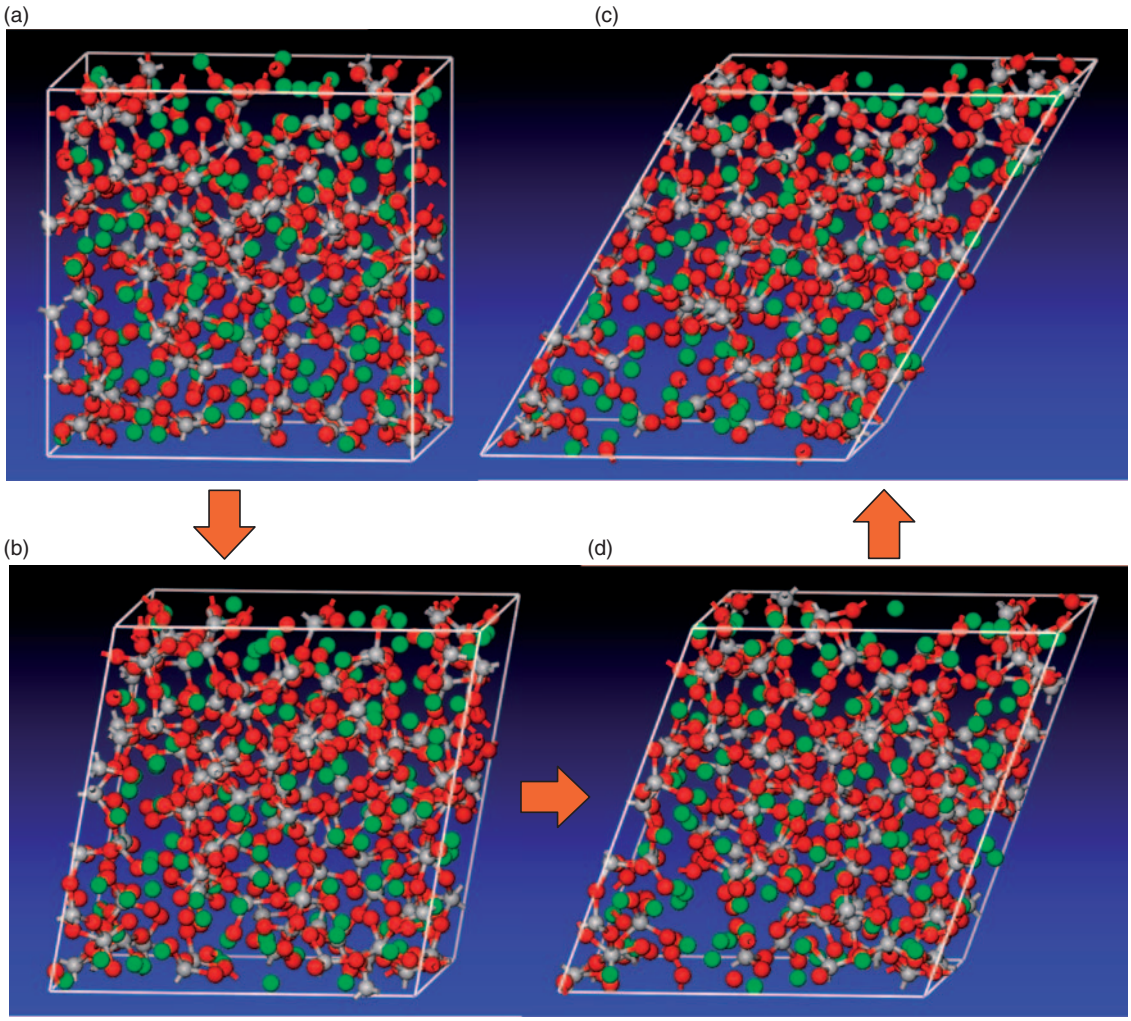

Fig. 6 An example of molecular-level topology evolution accompanying simple-shear mechanical tests. The tests were used to assess the extent of irreversible densification-induced strengthening of glass

4.1.4 Kinetics/dynamics of irreversible-densification processes

As correctly pointed out by one of the reviewers of this manuscript, the observed microstructural changes, which result in irreversible densification take place at room temperature. Conventionally, room temperature is considered to be associated with a low value of the material homologous temperature and, in the case of soda-lime glass, lies several hundreds of degrees below the glass-transition temperature.

Hence, it is quite unusual that significant microstructural changes can occur in soda-lime glass at room temperature. However, it should be recognized that, in the present case, the glass is subjected to high levels of pressure, which greatly increases the potential energy of this material in its original microstructural state. In other words, as the pressure is increased other microstructural states of glass become thermodynamically preferred. In the lower range of pressures, while the alternative microstructural states may be thermodynamically preferred, the presence of an activation-energy barrier prevents (except at sufficiently high temperatures) the phase transition of the material from its initial microstructural state to the thermodynamically preferred microstructural state. In the upper range of these pressures, on the other hand, the activation energy barrier disappears (at least, locally) so that the phase transition and the associated irreversible densification can take place at very high rates and without any assistance from thermal activation.

4.2 JH2 EOS and strength-model modifications

The molecular-level modelling results attained in the previous section were used to modify the original JH2 EOS and the strength model (as presented in section 3). A brief description of these modifications is given in the remainder of this section.

4.2.1 Modifications to the EOS

An examination of the polynomial EOS for glass as implemented in the ANSYS/Autodyn material library revealed that the extent of non-linearity is quite small, and hence, the P versus μ relationship was simplified using a linear EOS. In accordance with the results obtained in the previous section, the following additional simplifications/assumptions were made:

(a) the bulk modulus was assumed to take the same (constant) value in both the initial and compacted states of glass, as well as in all intermediate glass states;
(b) irreversible densification of glass is assumed to take place at a constant level of pressure.

In accordance with the molecular-level computational results presented in the previous section, this level of pressure was set to a value of 4 GPa.

A schematic of the changes made in the P versus μ relationship is given in Fig. 7. The aforementioned modifications in the JH2 EOS were implemented in the '*MDEOS_USER_1.f90*' material user subroutine which is then linked with ANSYS/Autodyn object code to form a new executable.

4.2.2 Modifications of the strength model

Irreversible densification of glass is assumed to increase its strength, both in the damage-free and the fractured states. This assumption is based on the following argument: in the case of the damage-free glass state, irreversible densification is assumed to repair molecular-level void-like regions. In the case of the fractured glass state, irreversible densification is assumed to act as a potent fragment-deformation mechanism resulting in mutually more-conformal fragments. The resulting increase in inter-fragment contact surface areas would then give rise to an increase in the friction-controlled strength of fractured glass. An examination of equations (26) and (27) revealed that the parameters A and B control glass strength in the two states, respectively. Following the aforementioned molecular-level findings regarding densification-induced strengthening of the glass, parameters A and B are increased by a factor of 1.5 for the fully densified glass material. At the intermediate levels of glass densification, parameters A and B are assumed to be linearly related to the degree of irreversible densification. The aforementioned modifications in the JH2 strength model were implemented in the '*MDSTR_USER_1.f90*' material user subroutine which is then linked with ANSYS/Autodyn object code to form a new executable.

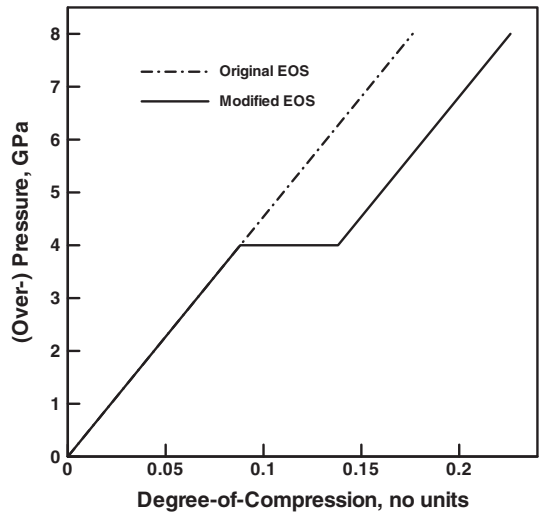

Fig. 7 A schematic the modifications made in the JH2 (over-pressure, P versus degree-of-compression, μ) EOS in order to account for the effect of high-pressure irreversible densification

4.3 Effect of high-pressure irreversible densification on ballistic-impact resistance of glass

In the previous section, the molecular-level computational results regarding high-pressure irreversible densification of glass were used to modify the EOS and the strength relations within the JH2 continuum

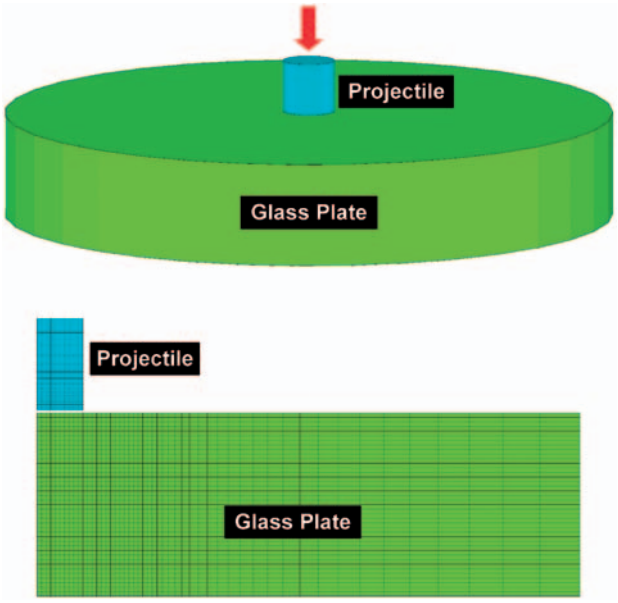

Fig. 8 (a) A schematic of the glass plate impacted by a solid right-circular cylindrical projectile and (b) an example of the computational mesh, based on the first-order four-node finite elements, used to model the projectile and the glass plate

model for this material. In this section, a simple transverse impact of a monolithic glass plate by a solid right-circular cylinder (FSP) is analysed computationally in order to assess if the aforementioned modifications in the JH2 model have any significant effect on the temporal evolution and spatial distribution of damage within the glass plate during impact and on the overall glass-plate penetration resistance.

4.3.1 Problem formulation

A schematic of a circular disc-shaped glass-plate (25.0 mm thick and 75.0 mm radius) impacted by an FSP (12.7 mm diameter and 12.7 mm length) problem is provided in Fig. 8(a). Owing to the attendant symmetry of the problem, an axisymmetric 2D formulation was employed. An example of the finite-element mesh based on the first-order four-node finite elements is displayed in Fig. 8(b). It is seen that a finer mesh is used in the FSP and in the region of the glass plate which is most severely affected during impact/penetration of the plate by the FSP.

The FSP is assumed to be made of AISI/SAE 4340 steel and this material is modelled using a linear EOS, the Johnson–Cook strength model, the Johnson–Cook failure model, and an erosion model based on the equivalent geometrical (i.e. elastic + plastic + crack) instantaneous strain. The details regarding formulation and parameterization of this model can be found in our previous work [**28**].

All the calculations carried out in this study were done using ANSYS/Autodyn, a general purpose nonlinear dynamics modelling and simulation software [**26**]. A transient non-linear dynamics problem is analysed within ANSYS/Autodyn by solving simultaneously the governing partial differential equations for the conservation of momentum, mass and energy along with the material-model equations and the equations defining the initial and the boundary conditions. The equations mentioned above are solved numerically using a second-order accurate explicit scheme and one of the two (Lagrange or Euler) basic mathematical approaches/processors. The key difference between the two processors is that within the Lagrange processor the numerical grid is attached to and moves along with the material during calculation while within the Euler processor, the numerical grid is fixed in space and the material moves through it. In this study, both the FSP and the glass plate are modelled using the Lagrange processor. In our recent work [**28**], a brief discussion was given of how the governing differential equations and the material-model relations define a self-consistent system of equations for the dependent variables (nodal displacements, nodal velocities, material-element densities, and material-element internal energy densities). In the same reference, a brief overview was provided of the contact/interaction and erosion algorithms implemented in ANSYS/Autodyn.

The initial conditions are defined is such a way that the FSP is assigned a downward velocity while the glass plate is assumed to be stationary. To reduce the effect of reflection of the shock waves at the (outer) hoop surface of the glass plate, the so-called 'transmit' boundary conditions were applied to all the nodes residing on this surface. The transmit boundary conditions enable propagation of the stress waves across the hoop surface without reflection [**28**].

4.3.2 Glass-plate impact computational results

An example of the results pertaining to the temporal evolution and spatial distribution of deformation and damage within the glass-plate and the FSP is displayed in Figs 9(a) to (d). Various deformation/failure models are colour coded to improve clarity of the results. The results displayed in Figs 9(a) to (d) show that shear-induced damage/failure is found mainly in the region underneath the FSP, tensile failure occurs at the glass-plate back-face (and is caused by reflection of the compressive stress wave at this face), and the FSP undergoes extensive plastic deformation (but little or no failure). These findings are fairly common and, hence, will not be discussed any further. It should be noted, however, that the results displayed in Figs 9(a) to (d) pertain to an FSP initial velocity of 600 m/s and the original (unmodified) JH2 glass-material model.

When the JH2 material model was modified to include the effect of high-pressure irreversible densification and the FSP initial velocity was maintained at 600 m/s, an identical temporal evolution and spatial distribution of the material deformation and failure was found as those in Figs 9(a) to (d). This finding was readily rationalized by establishing that the pressure within the glass-plate never reached the level of 4 GPa required for the irreversible densification to commence.

When the FSP velocity was increased to 1000 m/s, the effect of irreversible densification was observed. An example of this effect is given in Figs 10(a) and (b), in which distribution of deformation and damage within the glass-plate and the FSP are given for the cases of original and modified JH2 glass material models, respectively. The results displayed in these figures show that the extent of damage in the FSP increased, while that of damage in the glass-plate is reduced for the case of the modified JH2 material model. Also, the FSP exit velocity was found to be

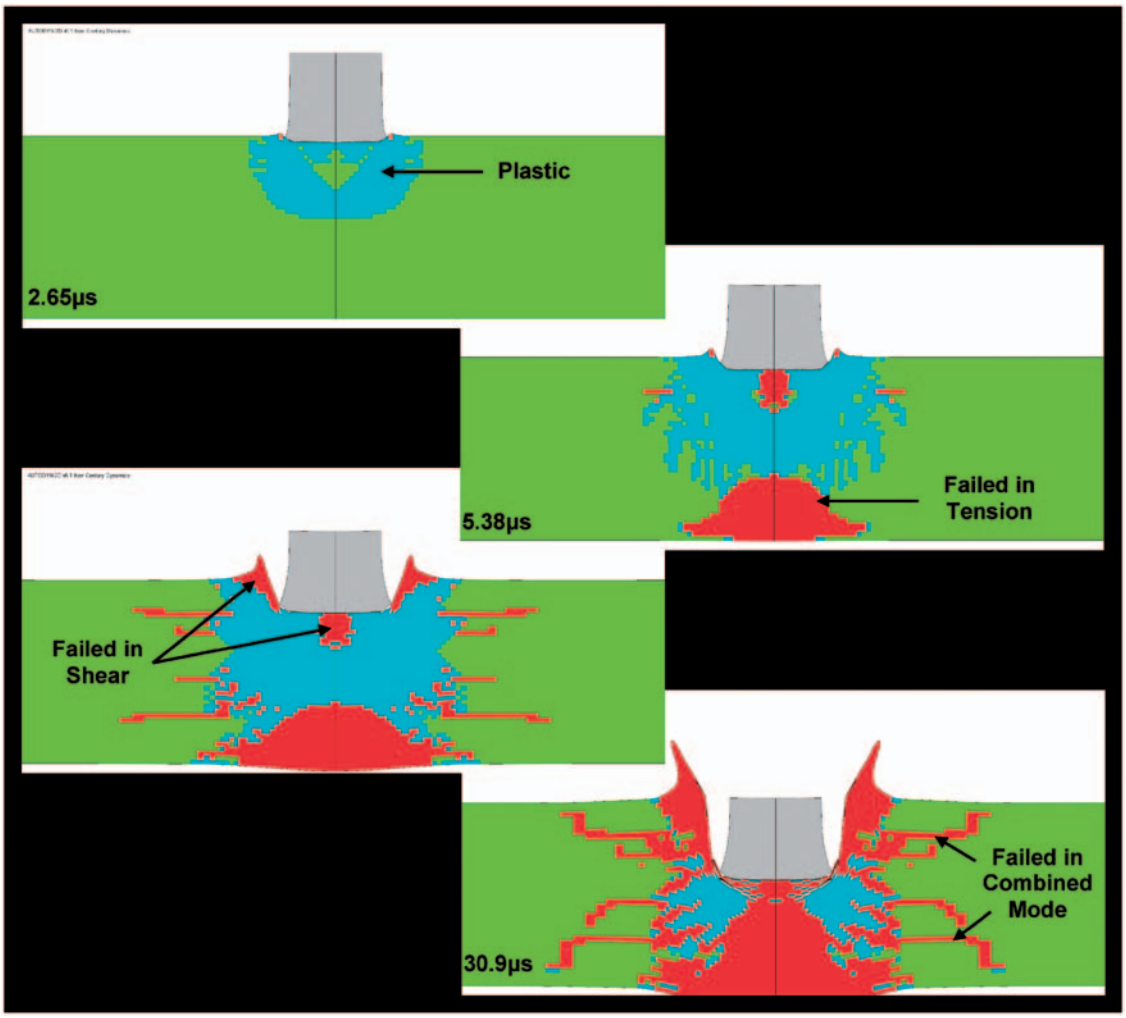

Fig. 9 An example of the results pertaining to the temporal evolution and spatial distribution of deformation and damage within the glass-plate and the FSP

reduced from 469.1 to 460.2 m/s as a result of glass material model modifications. This is a relatively small decrease (ca. 2 per cent) in the FSP residual velocity which may suggest that the irreversible compaction of glass may not be a potent ballistic-resistance enhancing mechanism in glass.

To further explore the effect of irreversible densification, a parametric study was set up in which the key parameters of this process were varied within physically realistic limits. Specifically, the pressure at which densification starts was varied in a range 1–10 GPa range, density increase between 5 and 15 per cent and the densification-induced strengthening extent (i.e. the multiplier of A and B parameters) in a 1.0–2.0 range. This study revealed that, at an FSP velocity of 1000 m/s, the FSP exit velocity can be reduced from 469.1 to 346.4 m/s (a 26 per cent reduction). The optimal set of irreversible-densification parameters was identified as: densification pressure 1 GPa, density increase 5 per cent, and a strengthening extent of 2.0. Figure 10(c) reveals spatial distribution of deformation/damage for the modified JH2 glass model and the optimal set of irreversible-densification parameters. It is seen that there is a significant reduction in damage to the glass material directly under the projectile due to the increased strength of the densified glass. This reduction in failed material under the projectile promotes an increase in the extent of plastic deformation experienced by the projectile which leads to spreading of its material over a larger area. These observed effects combine to allow for a significant decrease in the kinetic energy of the projectile with respect to the non-optimized glass material case.

Additional simulations were next carried out in order to establish if irreversible-compaction of glass (if associated with the aforementioned optimal set of parameters) can improve the ballistic-resistance of glass at lower FSP velocities. It was found that at an FSP initial velocity of 600 m/s, the FSP residual

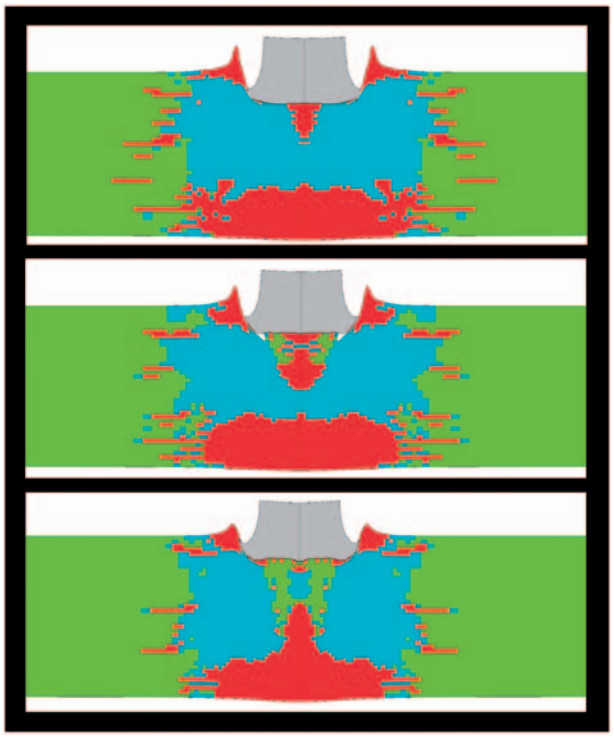

Fig. 10 The effect of the JH2 material-model modifications on the spatial distribution of damage within a soda-lime glass plate impacted with a 12.7-mm diameter/12.7-mm height solid right-circular cylinder at an initial velocity of 1000 m/s: (a) the original model; (b) the model modified using molecular-level finding; and (c) the modified using an optimal set of high-pressure irreversible-densification parameters

velocity was reduced from 240.4 to 154.2 m/s. Thus, if the irreversible-densification parameters of glass can be set to their optimal values, then the ballistic-penetration resistance can be improved for a range of FSP impact velocities.

4.3.3 Experimental validation

While there are numerous reports of experimental investigations aimed at assessing the ballistic performance of soda-lime glass [**12–15**, **31**], there are no open-literature reports regarding the operation or the role of irreversible densification in improving the ballistic performance of soda-lime glass. To address this problem, a companion experimental investigation is underway at the Army Research Laboratory, Aberdeen, Proving Ground, Maryland. Preliminary findings obtained in the post-mortem X-ray diffraction studies of glass fragments, carried out as part of this investigation, show the presence of a higher density soda-lime glass microstructural state and can be found in reference [**32**].

Table 1 Johnson–Holmquist 2 material model parameters for soda-lime glass

Parameter	Symbol	Unit	Value
EOS: linear			
Bulk modulus	K_1	Pa	4.54e10
Strength model: Johnson–Holmquist 2			
Shear modulus	G	Pa	3.04e10
HEL	σ_{HEL}	Pa	5.95e9
Intact strength constant	A	N/A	0.93
Intact strength exponent	N	N/A	0.77
Strain rate constant	C	N/A	0.003
Fractured strength constant	B	N/A	0.35
Fractured strength exponent	M	N/A	0.40
Max fracture strength ratio	–	N/A	0.50
Failure model: Johnson–Holmquist 2			
Hydro tensile limit	T	Pa	−3.5e7
Damage constant 1	D_1	N/A	0.053
Damage constant 2	D_2	N/A	0.85
Bulking constant	β	N/A	1.0

4.3.4 Materials-by-design approach

In summary, the results obtained in this study show that high-pressure irreversible densification of glass can become a potent ballistic-resistance enhancing mechanism provided (via chemical modifications, and various thermo-mechanical and chemical treatments) the densification parameters can be set to or near optimal values. In our ongoing work, molecular-level modelling is being extensively used to help better define such glass-modifying strategies/procedures. Specifically, within the molecular-level modelling framework, the effect of the glass chemistry and its random-network structure (as characterized by a set of random-network microstructural parameters [**29**, **30**]) on the irreversible-densification characteristics (i.e. the onset pressure and the extent of density change) is being examined. In addition, a link is being established between the molecular-level modelling parameters and the JH2 continuum-level material parameters. Table 1 summarizes the JH2 model parameters and lists their typical values for the case of a 'non-transforming' soda-lime glass. In this study, EOS is modified to account for the irreversible densification transition and two strength parameters (parameters A and B) were modified. In our on-going work, an attempt is being made to identify additional JH2 model parameters which require modifications as the soda-lime glass chemistry and the random-network structure are being modified. It is hoped that this will become a fruitful exercise of the so-called 'materials-by-design' concept in which component-level experimental and computational investigations are carried out in order to identify the envelope of optimal material properties. This is then followed by an extensive

experimental/computational procedure aimed at designing and synthesizing the materials with the targeted set of properties/performance attributes.

5 CONCLUSIONS

Based on the results obtained in this study, the following main conclusions can be made.

1. Molecular-level modelling of soda-lime glass revealed the occurrence of an irreversible-densification process when the pressure exceeds *ca.* 4 GPa. Close examination of molecular-level topology revealed that this process is associated with an increase in the average coordination number of the silicon atoms, and the creation of two to fourfold (smaller, high packing-density) Si–O rings.
2. Modifications of the continuum-level material model for glass to include the effect of irreversible densification resulted in minor improvements in the ballistic-penetration resistance of glass and only for high projectile initial velocities. Also, it is observed that the main threat to a soda-lime glass-based transparent-armour panel during the ballistic impact arises from the normal/tensile and less from deviatoric/shear stresses.
3. A parametric study involving variations of the key irreversible-densification parameters within physically realistic limits revealed that the optimal combination of these parameters can result in substantial improvements in the ballistic-resistance of glass over a wide range of projectile velocities.
4. It is suggested that various chemical-modification and thermo-mechanical treatment strategies should be employed in order to attain this optimal set of irreversible-densification parameters. This is an example of the materials-by-design concept within which an optimal combination of material parameters is identified in order to maximize component-level performance.

FUNDING

The material presented in this study is based on work supported by the U.S. Army/Clemson University Cooperative Agreements W911NF-04-2-0024 and W911NF-06-2-0042 and by an ARC-TARDEC research contract.

ACKNOWLEDGEMENTS

The authors are indebted to Dr. Georges Fadel for the support and a continuing interest in this work.

REFERENCES

1 **Strassburger, E., Patel, P., McCauley, W.,** and **Templeton, D. W.** Visualization of wave propagation and impact damage in a polycrystalline transparent ceramic- AlON. In Proceedings of the 22nd International Symposium on *Ballistics*, Vancouver, Canada, November 2005.
2 **AMPTIAC.** Army materials research: transforming land combat through new technologies. *AMPTIAC Qtly*, 2004, **8**(4), 11p.
3 **Strassburger, E., Patel, P., McCauley, J. W., Kovalchick, C., Ramesh, K. T.,** and **Templeton, D. W.** High-speed transmission shadow graphic and dynamic photoelasticity study of stress wave and impact damage propagation in transparent materials and laminates using the edge-on impact method. In Proceedings of the 23rd International Symposium on *Ballistics*, Spain, April 2007.
4 **Sun, D. Z., Andreiux, F.,** and **Ockewitz, A.** Modeling of the failure behavior of windscreens and component tests. In Proceedings of the 4th LS-DYNA Users' Conference, Bamberg, Germany, 23–25 May 2003.
5 **Woodcock, L. V., Angell, C. A.,** and **Cheeseman, P.** Molecular dynamics studies of the vitreous state: Simple ionic systems and silica. *J. Chem. Phys.*, 1976, **65**, 1565–1577.
6 **Valle, R. G. D.** and **Venuti, E.** High-pressure densification of silica glass: a molecular-dynamics simulation. *Phys. Rev. B*, 1996, **54**(6), 3809–3816.
7 **Trachenko, K.** and **Dove, M. T.** Densification of silica glass under pressure. *J. Phys. Condens. Matter*, 2002, **14**, 7449–7459.
8 **Liang, Y., Miranda, C. R.,** and **Scandolo, S.** Mechanical strength and coordinate defects in compressed silica glass: Molecular dynamics simulations. *Phys. Rev. B*, 2007, **75**, 024205.
9 **Nghiem, B.** *Fracture du verre et hétérogénéité à l'échelle submicronique*. PhD Thesis, University of Paris 6, France 1998.
10 **Denoual, C.** and **Hild, F.** Dynamic fragmentation of brittle solids: a multi-scale model. *Eur. J. Mech. Solids A*, 2002, **21**, 105–120.
11 **Yazdchi, M., Valliappan, S.,** and **Zhang, W.** A continuum model for dynamic damage evolution of anisotropic brittle materials. *Int. J. Numer. Meth. Eng.*, 1996, **39**, 1555–1583.
12 **Hild, F., Denoual, C., Forquin, P.,** and **Brajer, X.** On the probabilistic and deterministic transition involved in a fragmentation process of brittle materials. *Comput. Struct.*, 2003, **81**, 1241–1253.
13 **Grujicic, M., Pandurangan, B., Coutris, N., Cheeseman, B. A., Fountzoulas, C., Patel, P.,** and **Strassburger, E.** A ballistic material model for Starphire®, a soda-lime transparent-armor glass. *Mater. Sci. Eng. A*, 2008, **491**(1–2), 397–411.
14 **Grujicic, M., Pandurangan, B., Bell, W. C., Coutris, N., Cheeseman, B. A., Fountzoulas, C.,** and **Patel, P.** An improved mechanical material model for ballistic soda-lime glass. *J. Mater. Eng. Perform.*, 2009, **18**(8), 1012–1028.

15 **Grujicic, M., Pandurangan, B., Coutris, N., Cheeseman, B. A., Fountzoulas, C.,** and **Patel, P.** A simple ballistic material model for soda-lime glass. *Int. J. Impact Eng.*, 2009, **36**, 386–401.

16 **Holmquist, T. J., Templeton, D. W.,** and **Bishnoi, K. D.** Constitutive modeling of aluminum nitride for large strain high-strain rate, and high-pressure applications. *Int. J. Impact Eng.*, 2001, **25**, 211–231.

17 **Camacho, G. T.** and **Ortiz, M.** Computational modeling of impact damage in brittle materials. *Int. J. Solids Struct.*, 1996, **33**(20–22), 2899–2938.

18 **Sun, H.** COMPASS: an ab initio force-field optimized for condensed-phase applications overview with details on alkane and benzene compounds. *J. Phys. Chem. B*, 1998, **102**, 7338–7364.

19 **Sun, H., Ren, P.,** and **Fried, J. R.** The COMPASS force field: Parameterization and validation for phosphazenes. *Comput. Theor. Polym. Sci.*, 1998, **8**(1/2), 229–246.

20 Materials Studio 5.0, *Discover theory manual*, Accelrys Software Inc., 2009.

21 Materials Studio 5.0, *Visualizer manual*, Accelrys Software Inc., 2009.

22 Materials Studio 5.0, *Amorphouscell manual*, Accelrys Software Inc., 2009.

23 **Nose, S.** A unified formulation of the constant temperature molecular dynamics methods. *J. Chem. Phys.*, 1984, **81**, 511–519.

24 **Johnson, G. R.** and **Holmquist, T. J.** An improved computational constitutive model for brittle materials. *High pressure science and technology*, 1993 (AIP, New York).

25 **Holmquist, T. J., Templeton, D. W.,** and **Bishnoi, K. D.** Constitutive modeling of aluminum nitride for large strain high-strain rate, and high-pressure applications. *Int. J. Impact Eng.*, 2001, **25**, 211–231.

26 AUTODYN-2D and 3D. *Version 6.1*, *User documentation*, Century Dynamics Inc., 2006.

27 **Grujicic, M., Pandurangan, B.,** and **Zecevic, U.** Ballistic performance of alumina/S-2 glass-reinforced polymer-matrix composite hybrid lightweight armor against armor piercing (AP) and non-AP projectiles. *Multidiscipline Modeling Mater. Struct.*, 2007, **3**, 287–312.

28 **Grujicic, M., Pandurangan, B., Angstadt, C. D., Koudela, K. L.,** and **Cheeseman, B. A.** Ballistic performance optimization of a hybrid carbon nanotube/E-glass reinforced poly-vinyl-ester-epoxy matrix composite armor. *J. Mater. Sci.*, 2007, **42**, 5347–5349.

29 **Grujicic, M., Bell, W. C., Glomski, P. S., Pandurangan, B., Cheeseman, B. A., Fountzoulas, C.,** and **Patel, P.** Multi-length scale modeling of high-pressure induced phase transformations in soda-lime glass. *J. Mater. Eng. Perform.*, 2010. DOI: 10.1007/s11665-010-9774-2.

30 **Grujicic, M., Pandurangan, B., Bell, W. C., Cheeseman, B. A., Patel, P.,** and **Gazonas, G. A.** Molecular-level simulations of shock generation and propagation in soda-lime glass. *J. Mater. Sci.* 2011. DOI: 10.1007/s10853-011-5691-5.

31 **Bless, S.** and **Chen, T.** Impact damage in layered glass. *Int. J. Fract.*, 2010, **162**(1–2), 151–158.

32 **Gazonas, G. A., McCauley, J. W., Batyrev, I. G., Becker, R. C., Patel, P., Rice, B. M.,** and **Weingarten, N. S.** Multiscale modeling of noncrystalline ceramics (glass). ARL Technical Report, ARL-MR-0765, Aberdeen Proving Ground, February 2011.